

1 **Estimation of surface ammonia concentrations and emissions in**
2 **China from the polar-orbiting Infrared Atmospheric Sounding**
3 **Interferometer and the FY-4A Geostationary Interferometric**
4 **Infrared Sounder**

5 Pu Liu¹, Jia Ding¹, Lei Liu¹, Wen Xu², Xuejun Liu²

6 ¹ School of Earth and Environmental Sciences, Lanzhou University, Lanzhou 730000, China

7 ² College of Resources and Environmental Sciences, Center for Resources, Environment and Food Security, Key Laboratory
8 of Plant-Soil Interactions of MOE, China Agricultural University, Beijing 100193, China

9 Correspondence to: Lei Liu (liuleigeo@lzu.edu.cn)

10

11 **Abstract**

12 Ammonia (NH₃) is the most important alkaline gas in the atmosphere, which has negative effects on
13 biodiversity, ecosystems, soil acidification and human health. China has the largest NH₃ emissions
14 globally, mainly associated with agricultural sources including nitrogen fertilizer and livestock. However,
15 there is still a limited number of ground monitoring sites in China, hindering our understanding of both
16 surface NH₃ concentrations and emissions. In this study, using the polar-orbiting satellite (IASI) and
17 Fengyun-4 geostationary satellite (GIIRS), we analyzed the changes of hourly NH₃ concentrations, and
18 estimated surface NH₃ concentrations and NH₃ emissions in China. GIIRS-derived NH₃ concentrations
19 in the daytime were generally higher than that at night, with high values during 10:00-16:00. Satellite-
20 derived surface NH₃ concentrations were generally consistent with the ground observations with R-square

21 at 0.72 and slope equal to 1.03. Satellite-based NH_3 emissions ranged from 12.17-17.77 Tg N yr^{-1} during
22 2008-2019. Spatially, high values of NH_3 emissions mainly occurred in the North China Plain, Northeast
23 China and Sichuan Basin, while low values were mainly distributed in western China (Qinghai-Tibet
24 Plateau). Our study shows a high predictive power of using satellite data to estimate surface NH_3
25 concentrations and NH_3 emissions over multiple temporal and spatial scales, which provides an important
26 reference for understanding NH_3 changes over China.

27 **1 Introduction**

28 Ammonia (NH_3) is a highly active gas in the atmosphere and the most important alkaline gas, playing an
29 important role in atmospheric chemistry (Fowler et al., 2013). NH_3 reacts with acid pollutants (SO_2 and
30 NO_x) to form fine particulate matters, such as $\text{PM}_{2.5}$, leading to haze pollution. In addition, the deposition
31 of NH_3 and NH_4^+ could also cause environmental problems such as water eutrophication, biodiversity
32 loss and soil acidification (Paerl et al., 2014). China has become a major region for NH_3 emissions
33 globally, because of rapid growth of population and agricultural production (Zhang et al., 2017; Liu et al.,
34 2022). To provide a scientific basis for dealing with NH_3 pollution, it is urgent to accurately estimate both
35 surface NH_3 concentrations and emissions in China.

36

37 Surface NH_3 concentrations can be estimated by ground measurements and model simulations. Ground
38 measurements are considered to be the most accurate quantitative method. Current national NH_3
39 observation networks in China include the National Nitrogen Deposition Monitoring Network (NNDMN)
40 established by China Agricultural University (Xu et al., 2015) and the Ammonia Monitoring Network

41 (AMoN-China) established based on the Chinese Ecosystem Research Network (CERN) (Pan et al., 2018).
42 The NNDMN can measure ground NH₃ concentrations since 2010, while the AMoN-China only makes
43 the measurements in 2015-2016. The above two monitoring networks both monitor surface NH₃
44 concentrations on a monthly basis, and lack monitoring of the hourly NH₃ changes. Some studies have
45 conducted research on the intra-day/hourly changes of NH₃ concentrations based on ground observations.
46 Werner et al. (2017) measured hourly NH₃ concentration in 2012 at the Harwell site in the United
47 Kingdom, and found that high NH₃ concentration usually occurred in the afternoon. Similarly, Kutzner
48 et al. (2021) observed the hourly NH₃ concentration on the SIRTa Observatory in Paris and found NH₃
49 concentration was highest in the late afternoon. Pandolfi et al. (2012) studied the day-night cycle of NH₃
50 concentration at the two stations in Barcelona in summer, and found that the NH₃ concentration was
51 highly associated with local meteorology and traffic emissions. However, there are still a limited number
52 of monitoring sites on the hourly NH₃ changes in China.

53

54 Agricultural fertilizer and livestock production have led to a large amount of NH₃ emissions. China's
55 cultivated land area accounts for less than 10% of the world, but it consumes about 30% of the world's
56 nitrogen (N) fertilizer (Peng et al., 2002). Estimation of NH₃ emissions is mainly based on a bottom-up
57 method, using NH₃ source statistics (fertilization, animal husbandry, etc.) and emission factors. Zhou et
58 al. (2016) calculated the annual farmland NH₃ emission (3.96 ± 0.76 Tg N yr⁻¹) over China in 2008 based
59 on the bottom-up method, which was 40% higher than the emission in the Intergovernmental Panel on
60 Climate Change (IPCC) Tier 1 guidelines (2.89 Tg N yr⁻¹). Zhang et al. (2017) reassessed China's NH₃
61 emissions based on the mass balance method, and found NH₃ emissions increased from 12.1 ± 0.8 in 2000

62 to 15.6 ± 0.9 Tg N yr⁻¹ in 2015, with an annual growth rate of 1.9% . Fu et al. (2020) estimated that
63 China's NH₃ emissions increased from 4.7 in 1980 to 11 Tg N yr⁻¹ in 2016. Although many studies
64 regarding NH₃ emissions have been carried out in China, great uncertainties and large ranges (7-16 Tg N
65 yr⁻¹) still existed in the estimates of China's NH₃ emissions (Dong et al., 2010; Huang et al., 2012; Kang
66 et al., 2016).

67

68 Besides the bottom-up estimates, some studies used data assimilation methods by ground monitoring data
69 to constrain NH₃ emission estimates. Paulot et al. (2014) assimilated the GEOS-Chem with ground
70 observations of wet N_r deposition, and estimated China's NH₃ emission as 8.4 Tg N yr⁻¹ in 2008 with
71 seasonal NH₃ emission peaked in summer. Gilliland et al. (2003) used the data assimilation method by
72 the Community Multiscale Air Quality (CMAQ) with the wet NH₄⁺ concentration data from the USA
73 National Atmospheric Deposition Program Network, and found that obvious seasonal differences
74 appeared in NH₃ emissions linked to N fertilizer and temperature. Kong et al. (2019) carried out inversion
75 through assimilating surface AMoN NH₃ observation data, and improved the accuracy of temporal and
76 spatial pattern of NH₃ emissions in China.

77

78 In recent years, atmospheric remote sensing has developed rapidly, which can monitor NH₃ at a global
79 scale including the polar-orbiting satellite instruments such as the Tropospheric Emission Spectrometer
80 (TES), Infrared Atmospheric Sounding Interferometer (IASI), Cross-track Infrared Sounder (CrIS),
81 Atmospheric Infrared Sounder (AIRS), and Greenhouse Gases Observing Satellite (GOSAT) (Someya et
82 al., 2020). Many studies have reported the effectiveness of using satellite data to study NH₃ dynamics.

83 Pinder et al. (2011) found that TES observation can capture spatial-temporal NH₃ patterns compared with
84 surface measurement; Van Damme et al. (2014) studied the seasonal and annual NH₃ changes in the
85 northern and southern hemisphere using the IASI NH₃ column data, and found that the seasonality in the
86 southern hemisphere is mainly related to biomass burning; Shephard and Cady-Pereira (2015) developed
87 the CrIS NH₃ inversion algorithms, and found that CrIS can capture the global spatial distribution of NH₃
88 concentration; Warner et al. (2016) identified the main hotspots of agricultural NH₃ regions using AIRS,
89 such as South Asia, China, the United States and some parts of Europe, and found that NH₃ concentrations
90 increased at these agricultural regions since 2003. Besides, some studies also used the satellite
91 measurements to improve the estimates of NH₃ emissions. Zhang et al. (2017) developed a top-down
92 inversion method using TES NH₃ observation to quantify China's NH₃ emission, and obtained annual
93 NH₃ emission as 11.7 Tg N yr⁻¹ in 2008. Marais et al. (2021) estimated NH₃ emissions in the UK based
94 on IASI and CrIS and found the relative errors of IASI-derived NH₃ emissions were 11-36% and 9-27%
95 respectively; Van Damme et al. (2018) used the high-resolution IASI NH₃ maps to identify, classify and
96 quantify NH₃ emission hotspots in the world, which was helpful to understand the man-made point NH₃
97 sources; Dammers et al. (2019) identified global 249 NH₃ emission point sources based on CrIS, whose
98 total emission was about 2.5 times higher than that reported in the HTAPv2 emissions.

99

100 Besides the polar-orbiting satellite, China's Geostationary Interferometric Infrared Sounder (GIIRS)
101 onboard the Chinese FY-4A satellite can measure hourly changes of atmospheric NH₃ almost all of Asia
102 per day, which provides great potential to study the diel cycle of NH₃. In this study, GIIRS is used to
103 study the NH₃ diel cycle (hourly changes), which is essential for understanding the differences between

104 different times in a day by the polar-orbiting satellites (such as IASI at 9:30 and CrIS at 13:30). Second,
105 the surface NH_3 concentration in China is estimated based on both GIIRS and IASI, which is then
106 compared with the NNDMN. Third, NH_3 emission in China is calculated based on satellite-derived
107 surface NH_3 concentration and the feedback relationship between surface NH_3 concentration and emission
108 by a chemistry transport model (GEOS-Chem). Finally, the spatial-temporal characteristics of satellite-
109 derived surface NH_3 concentration and emission are analyzed, and the uncertainties are discussed.

110 **2 Data and methods**

111 **2.1 Satellite GIIRS NH_3**

112 The Geostationary Interferometric Infrared Sounder (GIIRS) onboard the Fengyun-4A geostationary
113 satellite (FY-4A) launched by China in 2016 is the world's first hyperspectral atmospheric infrared
114 sounder (Cai et al., 2020). The FY-4A GIIRS detected spectral range is $700\text{-}2250\text{ cm}^{-1}$, including 1648
115 spectral channels and 14 radiations imaging channels, covering visible light, short, medium and long wave
116 infrared bands. The spatial resolutions of the detector are 2.0 km in the visible bands and 16 km in the
117 infrared bands. It covers almost the whole of Asia and scans 10 times a day (Zhang et al., 2019). The
118 GIIRS can detect the temperature and humidity profiles and trace gases at high frequencies.

119

120 NH_3 has two large absorption characteristics in the long wave infrared (about 930 cm^{-1} and 965 cm^{-1}).
121 The contribution of NH_3 to the brightness temperature of these two bands is between 2-4 k. The core of
122 inversion algorithms is based on the so-called hyperspectral radiation index (HRI), which quantifies the
123 spectral characteristics of NH_3 . The HRI index depends on whether the satellite instrument detects the

124 presence of NH₃. The average value of HRI is 0 with a standard deviation of 1, and the HRI range is [-
125 1,1]. The algorithm for estimating IASI NH₃ column concentration is to convert HRI into a column using
126 the so-called neural network (Clarisse et al., 2021).

127

128 In this study, we use hourly NH₃ concentrations during 2019-2020 (from November 2019 to October
129 2020) to study NH₃ diel cycle with a resolution of 0.5 °. The original data is in H5 format, and the unit of
130 NH₃ is molecules cm⁻². The data is processed with MATLAB software. First, observations with
131 considerable uncertainties (relative error exceeds 50%) and high clouds (cloud cover exceeds 20%) are
132 removed (Fig. S1a). Secondly, the world standard time (UTC) by GIIRS is converted to local time, and
133 the data in H5 format is converted to TIFF data.

134 **2.2 Satellite IASI NH₃**

135 IASI instrument is on board the polar solar synchronous Metop-A platform. It has been running stably
136 since 2006 to measure the infrared radiation emitted by the earth (Van Damme et al., 2014). IASI can
137 measure the infrared radiation emitted by the earth's surface and atmosphere in the spectral range of 645-
138 2760 cm⁻¹. It can observe the world twice a day, and cross the equator at 9:30 and 21:30 local time, with
139 a spatial resolution of 12 km at nadir. However, only daytime satellite measurements are used, because
140 nighttime measurements usually have greater uncertainties related to thermal contrasts (Van Damme et
141 al., 2017).

142 The near-real time dataset of the total NH₃ column (ANNI-NH₃-v3) was used here. The properties of IASI
143 NH₃ data include NH₃ column concentration, longitude, latitude, measurement time, cloud cover,
144 uncertainty, solar zenith angle and other parameters. The daily NH₃ column from 2008 to 2019 was used.

145 The format of the original data is NC format, and the unit is mol m⁻². The observation data with cloud
146 cover larger than 20% and the uncertainty above 50% were removed (Fig. S1b). We gridded the data to
147 0.1 °by using the arithmetic average methods.

148 **2.3 Ground NH₃ measurements**

149 Surface NH₃ concentrations in the NNDMN were used to compare with the satellite estimates including
150 43 observation stations. The land types of the NNDMN sites cover cities, farmland, coastal areas, forests
151 and grasslands. Measurements during the period from January 2010 to December 2015 by the NNDMN
152 were used. Surface NH₃ concentrations were measured using an active DELTA (DEnuder for Long-Term
153 Atmospheric sampling) (Flechard et al., 2011). For the hourly measurements, we collected the data from
154 the published papers including 5 sites (Table S1) including Xianghe (39.75 °N, 116.96 °E, 2017.12 -2018.2)
155 (He et al., 2020), Fudan University (31.30 °N, 121.50 °E, 2013.7.1-2014.9.30) (Wang et al., 2015),
156 Dianshan Lake (31.09 °N, 120.98 °E, 2013.7.1-2014.6.30) (Wang et al., 2015), Jinshan Chemical Industry
157 Park (30.73 °N, 121.27 °E, 2014.1.6-2014.6.30) (Wang et al., 2015), and Gucheng (39.15 °N, 115.73 °E,
158 2016.3-2017.5) (Kuang et al., 2020). The Xianghe site in Hebei Province and Dianshan Lake site in
159 Shanghai represent rural environments; Jinshan Chemical Industry Park represents industrial
160 environments; Gucheng site in Hebei and the Fudan University site in Shanghai represent urban
161 environments.

162 **2.4 GEOS-Chem**

163 The GEOS-Chem model version 12.3.0 is a three-dimensional chemistry transport model developed by
164 Harvard University, which has been widely used in the field of atmospheric studies (Eastham et al., 2014).

165 The nested regional model in Asia was used in this study driven by assimilated GEOS-5 meteorological
166 data at a horizontal resolution of $1/2^\circ \times 2/3^\circ$. Dry deposition calculation in GEOS-Chem follows a
167 standard resistance-in-series model (Wesely, 2007), while wet deposition includes both convective
168 updraft and large-scale precipitation scavenging (Jacob, 1999). The GEOS-Chem model here does not
169 consider land-atmosphere bi-directional NH_3 exchange, and the NH_3 flux was parameterized as uncoupled
170 emission and dry deposition processes. Anthropogenic emissions over China were from the Regional
171 Emission in Asia (REAS-v2) inventory. The GEOS-Chem outputs of NH_3 concentrations include 47
172 layers from the ground to the top of atmosphere, which were used to capture NH_3 vertical profiles. The
173 feedback between surface NH_3 concentration and emissions was also calculated by GEOS-Chem.

174 **2.5 Satellite-based surface NH_3 estimates and emissions**

175 Surface NH_3 concentrations were estimated using the satellite NH_3 columns as well as NH_3 vertical
176 profiles. To gain the continuous vertical NH_3 profile, the Gaussian function was used to fit the 47 layers'
177 NH_3 concentrations. A three parameter Gaussian function was used to fit NH_3 vertical profiles at each
178 grid box from GEOS-Chem according to previous studies (Liu et al., 2019).

$$179 \quad \rho(Z) = \sum_{i=1}^n \rho_{\max,i} e^{-\left(\frac{Z-Z_{0,i}}{\sigma_i}\right)^2}, \quad (1)$$

180 where Z is the height of a layer in the atmospheric chemical transport modeling (ACTM); ρ_{\max} , Z_0 and σ
181 are the maximum of NH_3 concentration, the corresponding height with the maximum of NH_3
182 concentration and the thickness of NH_3 concentration layer (one standard error of Gaussian function).

183

184 The satellite-derived NH_3 concentration at the height of h_G can be calculated as:

185
$$S_{G_NH_3} = S_{trop} \times \frac{\rho(h_G)}{\int_0^{h_{trop}} \rho(Z) dx} \times \frac{G_{ACTM}^{1-24}}{G_{ACTM}^{overpass}}, \quad (2)$$

186 where $\frac{\rho(h_G)}{\int_0^{h_{trop}} \rho(Z) dx}$ represents the ratio of NH₃ concentration at the height of h_G to total columns

187 ($\int_0^{h_{trop}} \rho(Z) dx$); S_{trop} represents satellite-derived NH₃ columns; $\frac{G_{ACTM}^{1-24}}{G_{ACTM}^{overpass}}$ is the ratio of average surface

188 NH₃ concentration (G_{ACTM}¹⁻²⁴) to that at satellite overpass time (G_{ACTM}^{overpass}) by an ACTM.

189

190 The mass balance method (Lamsal et al., 2011; Geddes and Martin, 2017; Cooper et al., 2017) was used

191 to exploit the feedback ratio of surface NH₃ concentrations and NH₃ emissions (Marais et al., 2021):

192
$$E_s = S_{G_NH_3} \times \left(\frac{E}{G_{G_NH_3}_m} \right), \quad (3)$$

193 where E_s is satellite-based NH₃ emissions; S_{G_NH₃} is the satellite-derived surface NH₃ concentrations;

194 $\left(\frac{E}{G_{G_NH_3}_m} \right)$ is the ratio of surface NH₃ concentrations and NH₃ emissions simulated by the GEOS-Chem.

195 **3 Results and discussions**

196 **3.1 GIIRS-based hourly NH₃ concentrations during 2019-2020**

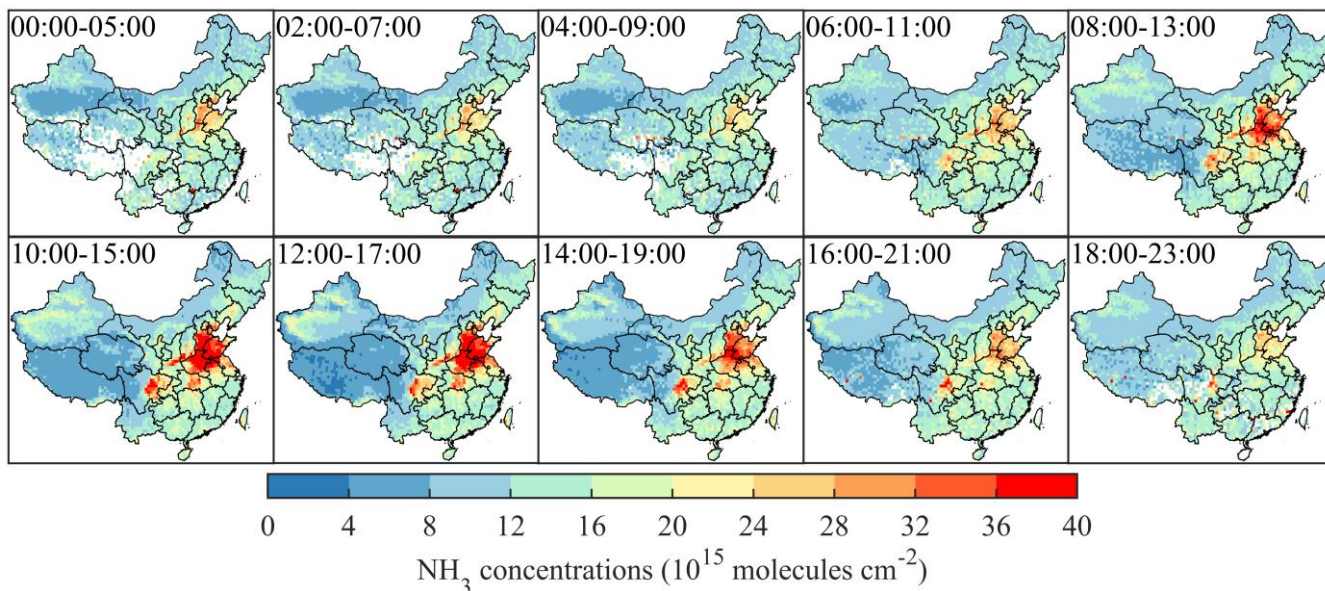
197 Fig. 1 shows the hourly NH₃ concentrations observed from GIIRS during 2019-2020. Daytime NH₃

198 columns were significantly higher than those at night. The intra-day hourly NH₃ columns showed an

199 overall increase first, then a decrease, with high values during 10:00-16:00. The increase in temperature

200 enhanced the volatilization of NH₃, which may explain high values of NH₃ concentrations during the

201 daytime.



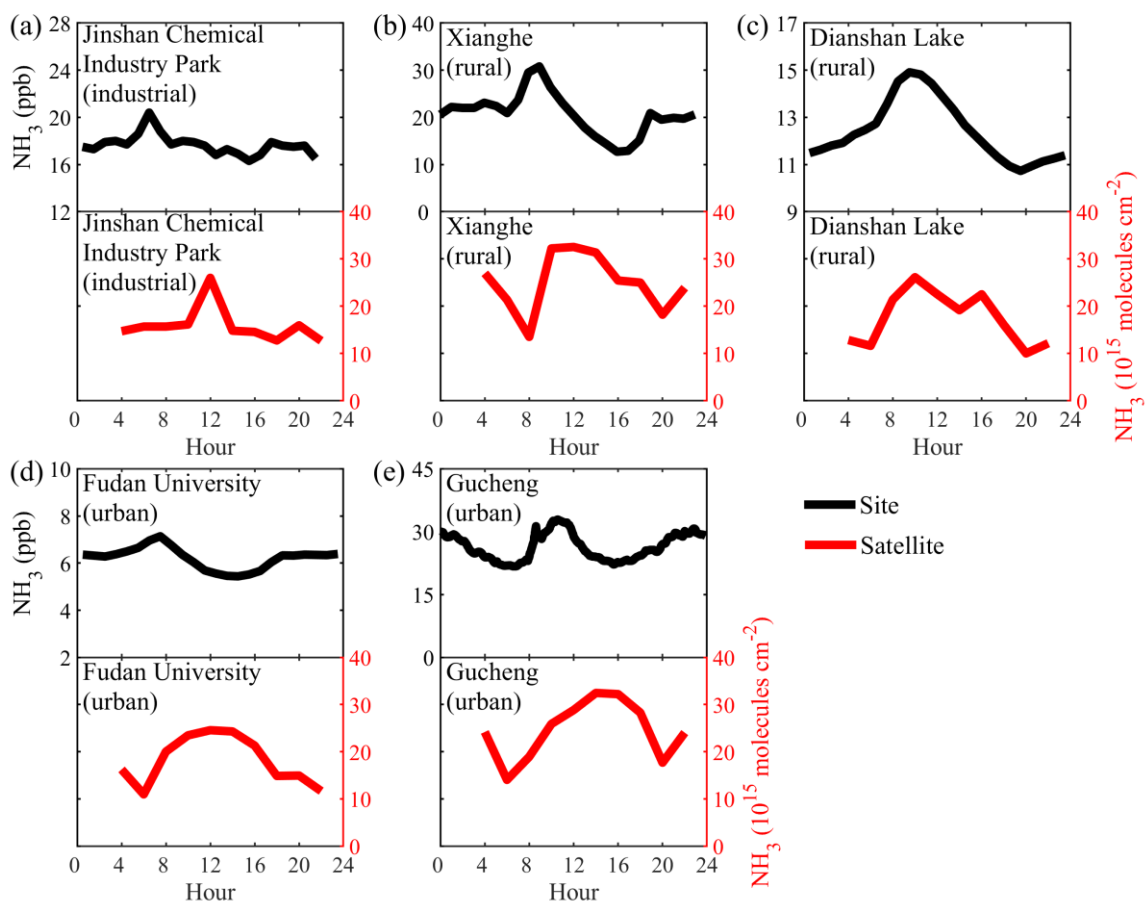
202

203 **Figure 1.** Monthly average NH_3 concentrations for each of the 10 GIIRS overpass time periods during
 204 2019-2020.

205 Ground-based measurements of hourly NH_3 concentrations are very lacking, and the timespan may be
 206 different from GIIRS measurements. Here we only used them to show the hourly patterns of NH_3
 207 concentrations (Fig. 2). The Xianghe site in Hebei Province and Dianshan Lake site in Shanghai represent
 208 rural environments; Jinshan Chemical Industry Park represents industrial environments; Gucheng site in
 209 Hebei and the Fudan University site in Shanghai represent urban environments.

210 NH_3 concentration in the rural environment basically shows a normal distribution, and high NH_3
 211 concentration generally appears between 9:00-16:00, which may be related to agricultural activities and
 212 temperature. In the industrial environment (Jinshan Chemical Industry Park, JSP), NH_3 concentration
 213 fluctuates irregularly, and two peaks appear at 12:00 and 6:00-8:00, while NH_3 concentration tends to be
 214 stable at other times. In the urban environment, the changes in NH_3 concentration by satellite at the
 215 Gucheng site are consistent with ground monitoring, showing a clear peak around 9:00-14:00; NH_3

216 concentration at the Fudan University site gradually decreases from the morning peak to the afternoon.
 217 The evaporation of dew may drive the NH_3 increase from the morning to the noon (Wang et al., 2015).
 218 NH_3 concentration by ground monitoring in cities (Gucheng and Fudan University) has double peaks
 219 between 8:00-11:00 and 18:00-22:00, which may also be related to traffic emissions. In summary, except
 220 for industrial sites, hourly NH_3 in China has a large variability between day and night and the hourly NH_3
 221 patterns are affected by many factors, of which anthropogenic emissions and temperature seem to be the
 222 most important driving factors.

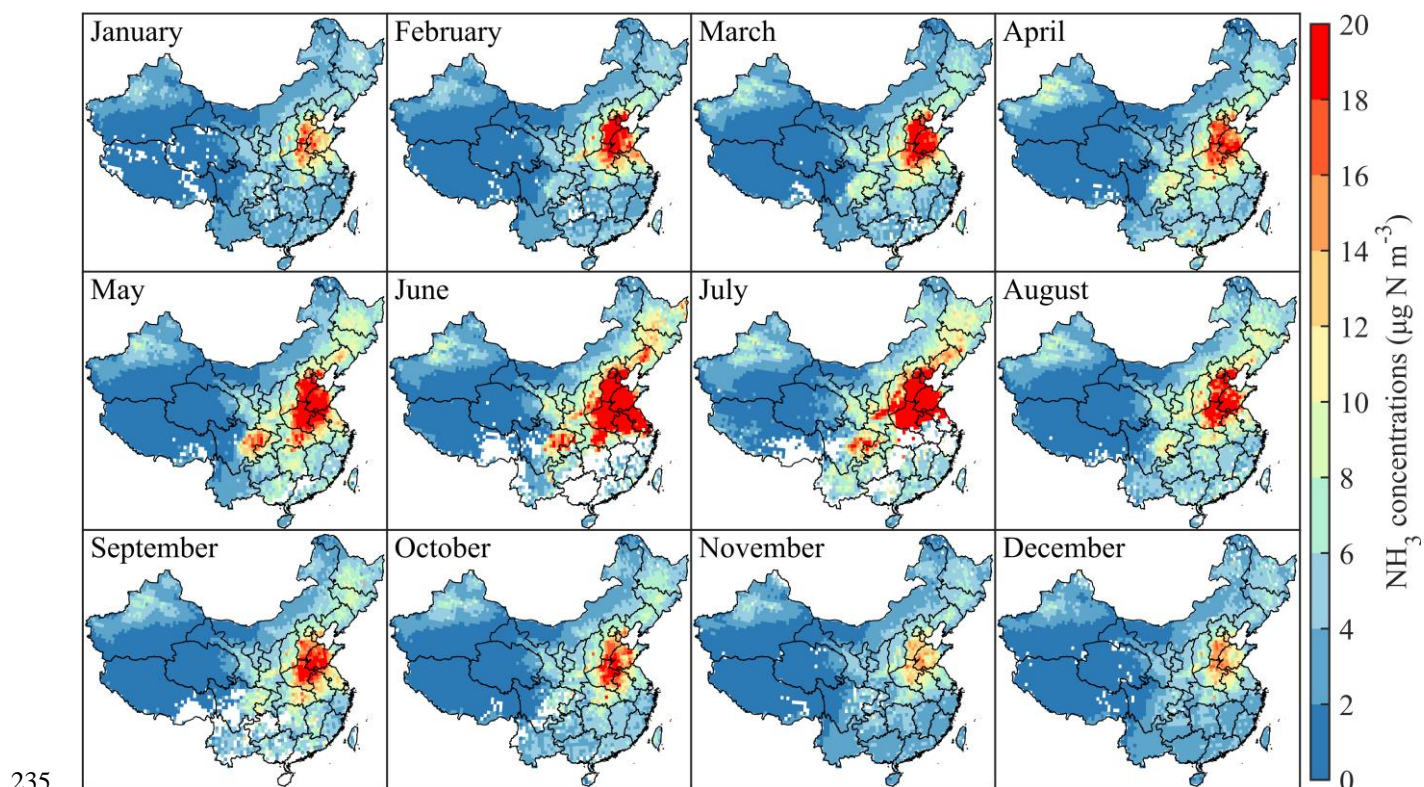


223

224 **Figure 2.** GIIRS-based and measured hourly NH_3 concentrations at five sites including Jinshan Chemical
 225 Industry Park (JSP, a), Xianghe (XH, b), Dianshan Lake (DSL, c), Fudan University (FDU, d) and

226 Gucheng (GC, e).

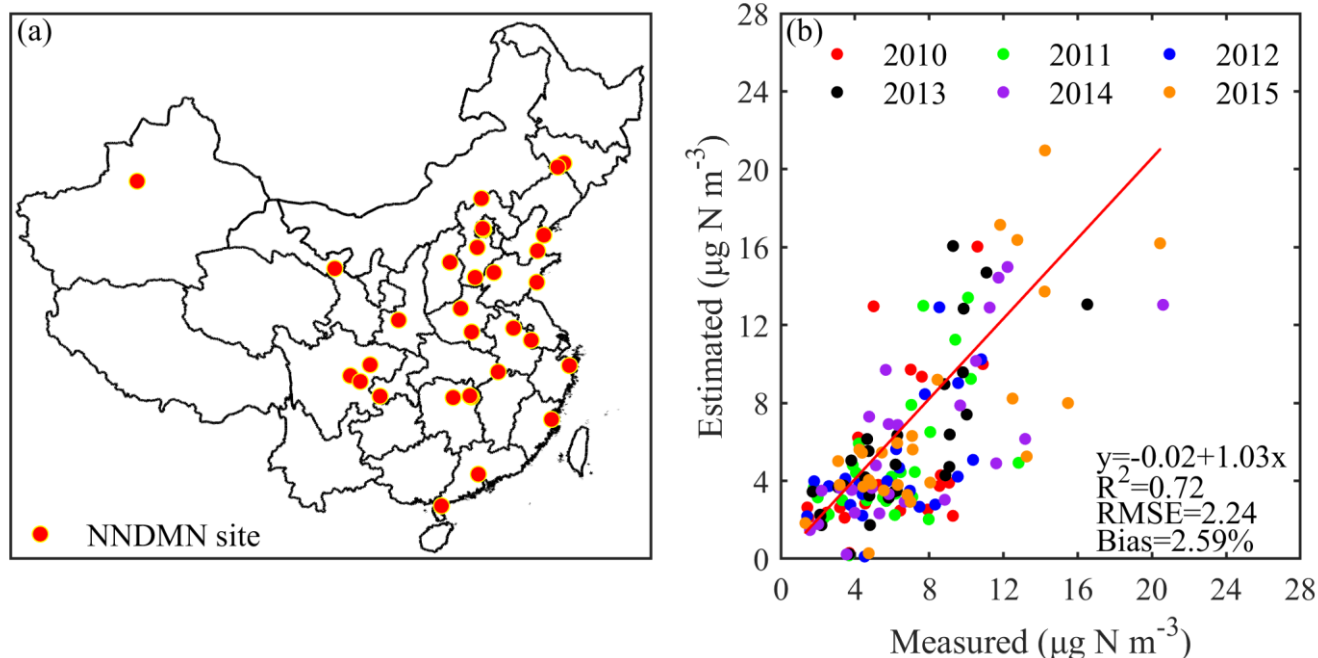
227 Spatial distribution of GIIRS-based surface NH_3 concentrations across China had large variability. High
228 surface NH_3 concentration ($>10 \mu\text{g N m}^{-3}$) is mainly concentrated in the North China Plain (NCP),
229 followed by the Sichuan Basin, Northeast China and parts of Xinjiang, while low values ($<4 \mu\text{g N m}^{-3}$)
230 are mainly concentrated in the Qinghai-Tibet Plateau. High surface NH_3 concentration ($126.85 \mu\text{g N m}^{-3}$)
231 appears in July ($6.78 \mu\text{g N m}^{-3}$ as average), and the lowest value ($0.23 \mu\text{g N m}^{-3}$) appears in November
232 ($3.25 \mu\text{g N m}^{-3}$ as average). There are obvious seasonal changes in surface NH_3 concentrations in the NCP
233 with high values in summer, and low values in winter, related to both agricultural N fertilizer and higher
234 temperature.



236 **Figure 3.** Spatial distribution of monthly surface NH_3 concentrations in China by GIIRS in 2019-2020.

237 **3.2 IASI-based NH₃ surface concentrations**

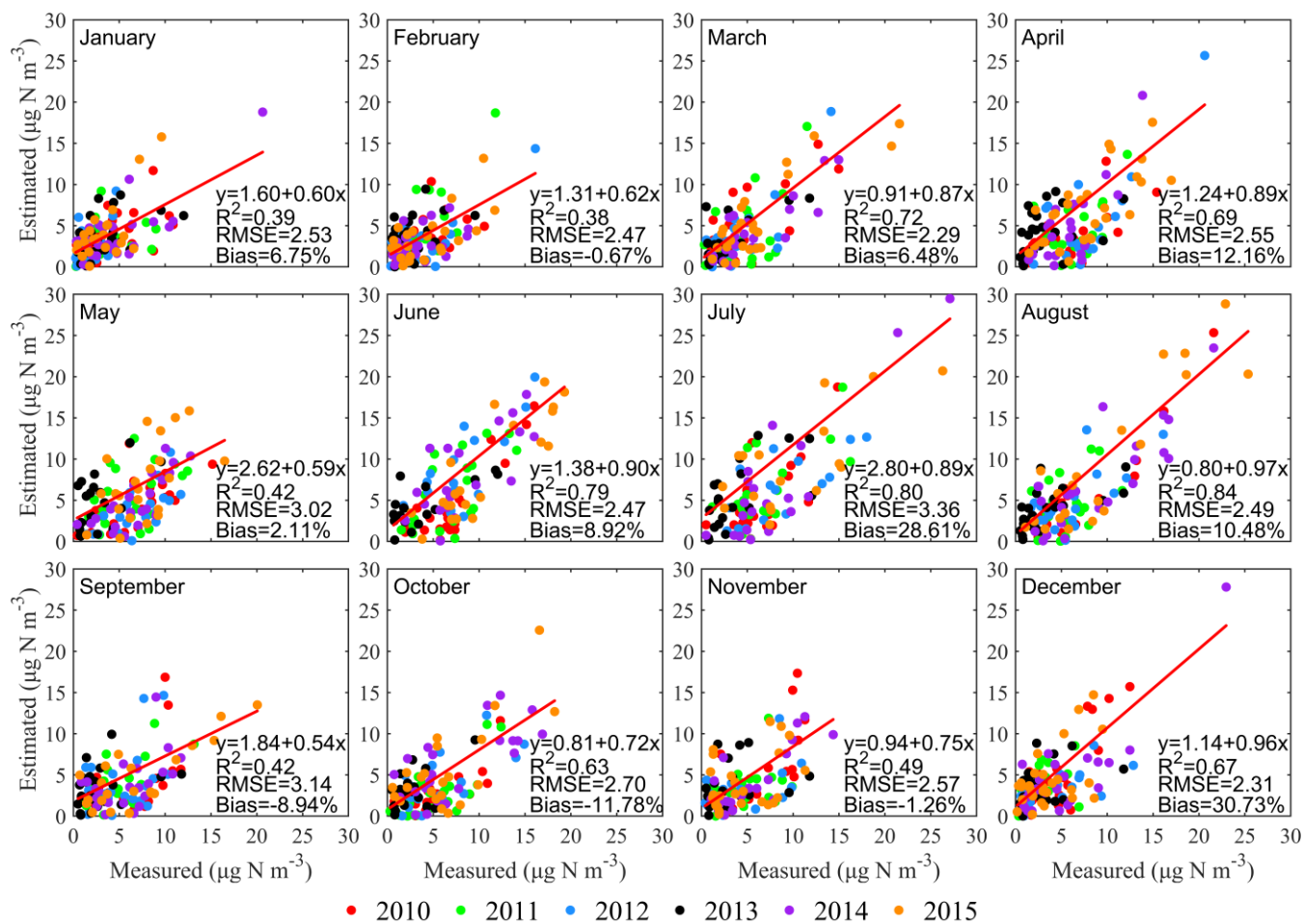
238 The observation data of the NNDMN in China was collected to compare with IASI-derived surface NH₃
239 concentration. In general, a good consistency was found between measurements and satellite estimates
240 with the regression R² as 0.72 and the RMSE as 2.24 μg N m⁻³. The coefficient of the fitted line was
241 1.03≈1 and the bias was 2.59%.



242
243 **Figure 4.** Comparison of IASI surface NH₃ concentrations with NNDMN measurements. (a) The
244 locations of NNDMN; (b) the regression results between satellite-estimates and measurements.

245
246 Monthly regression R² between the satellite-derived NH₃ concentration and the measured NH₃ was 0.38-
247 0.84. The regression R² reached the higher value (>0.80) in July and August. The RMSE ranged from
248 2.29- 3.36 μg N m⁻³, which reached the maximum value of 3.36 μg N m⁻³ in July, and reached the smallest
249 in March (2.29 μg N m⁻³). The bias is basically less than 31% for all months, and reached the minimum

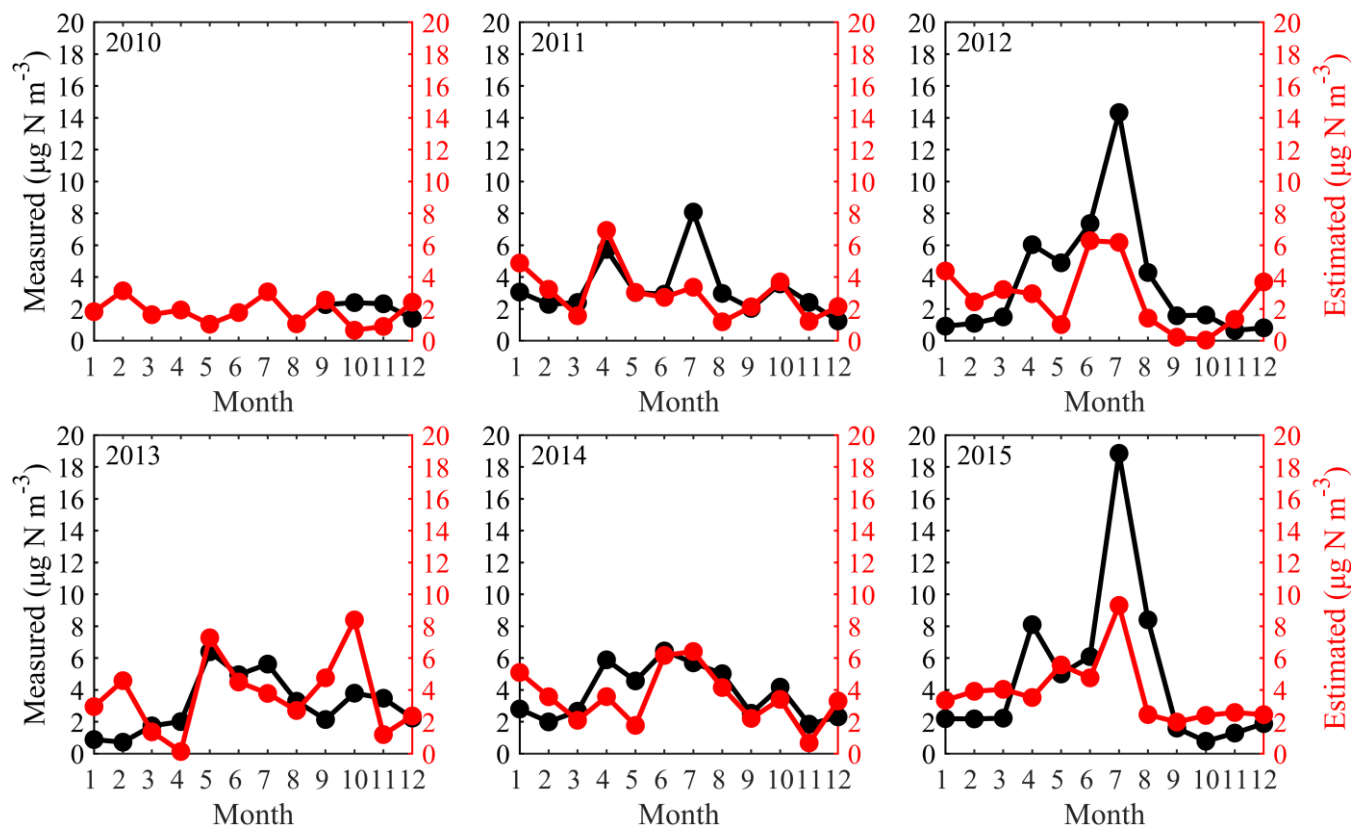
250 value of 0.67% in February, indicating that the monthly IASI-derived surface concentration obtained are
 251 consistent with measurements.



253 **Figure 5.** Comparison of monthly average values of IASI-derived and observed NH₃ surface
 254 concentrations in 2010-2015.

255
 256 Fig. 6 shows the monthly changes of surface NH₃ concentrations in Huinong County in Ningxia from
 257 2010 to 2015 for a total of 72 months. Surface NH₃ concentrations retrieved by IASI were compared with
 258 the observation data at Huinong. The highest value of each year basically appeared from June to August,

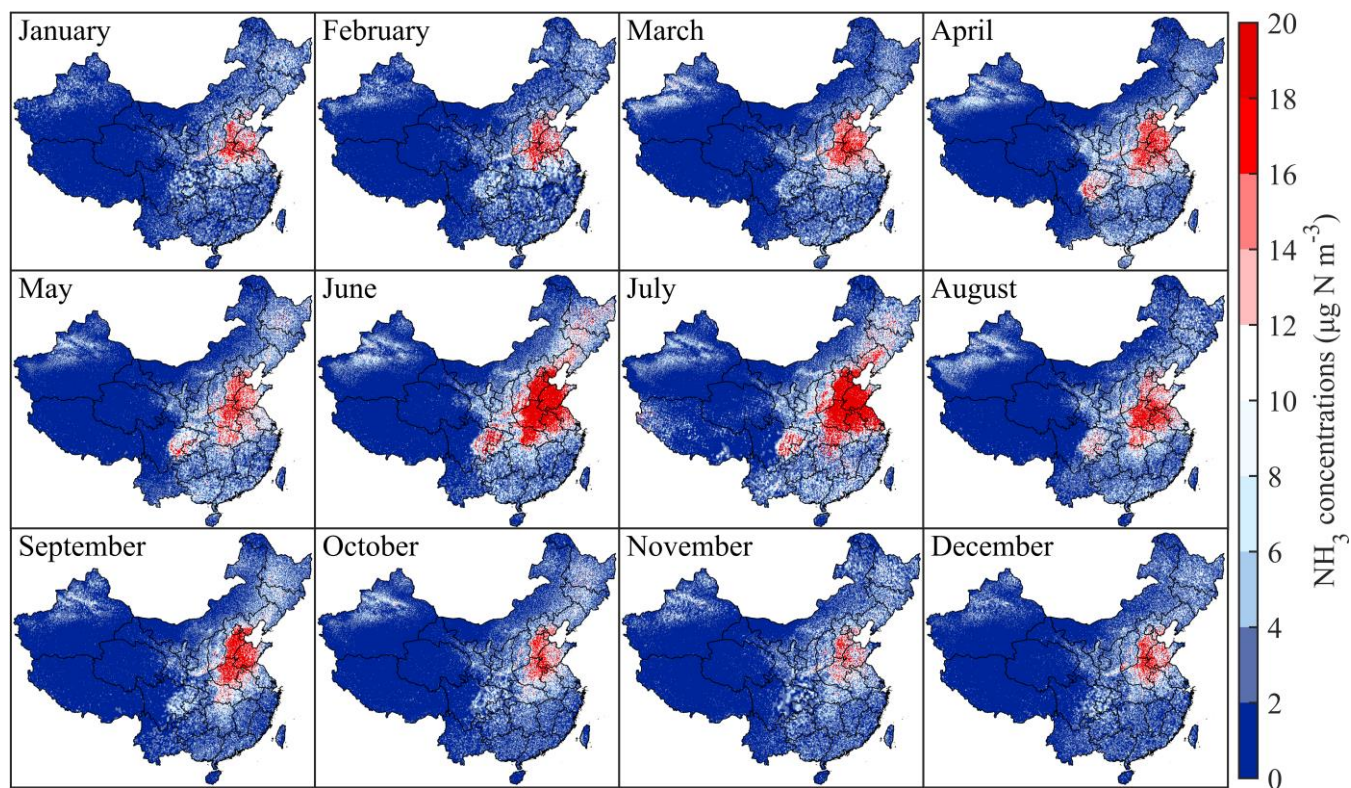
259 and the lowest values appeared from December to January. In the past 6 years, the maximum measured
 260 NH_3 concentration appeared in June 2015 ($18.9 \mu\text{g N m}^{-3}$), and the minimum appeared in November 2012
 261 ($0.6 \mu\text{g N m}^{-3}$). The observation data and satellite data have the same seasonal changes.



262
 263 **Figure 6.** Monthly changes of NH_3 concentrations in Huinong County in Ningxia from 2010 to 2015 for
 264 a total of 72 months during 2010-2015.

265
 266 Fig. 3 and Fig. 7 show the spatial distribution of GIIRS-derived and IASI-derived surface NH_3
 267 concentrations in 2019. The spatial distribution and gradients of surface NH_3 concentrations by the GIIRS
 268 and IASI have the same gradients from eastern to western regions. One notable difference occurred in the

269 middle and lower reaches of the Yangtze River in June and July since the GIIRS observations are affected
270 by clouds and had missing data.



271

272 **Figure 7.** Spatial distribution of monthly surface NH₃ concentrations in China by IASI in 2019.

273

274 3.3 IASI-derived NH₃ emissions

275 Based on the top-down estimates, China's NH₃ emissions ranged from 12.17-17.77 Tg N yr⁻¹ during
276 2008-2019. From 2008 to 2015, NH₃ emissions increased from 13.00 Tg N yr⁻¹ to 17.06 Tg N yr⁻¹. Since
277 2008, the temperature in China has risen steadily (Ding et al., 2007), promoting the volatilization of NH₃,
278 which partly explains the increase in NH₃ emissions from 2008 to 2015. After 2015, NH₃ emissions
279 fluctuated and changed slightly (16.08-17.77 Tg N yr⁻¹). Compared with other studies, the change in NH₃
280 emissions from 2008 to 2015 is consistent with previous estimates, and the overall NH₃ emissions show

281 an upward trend (Kang et al., 2016; Zhang et al., 2018; Ma, 2020; Fu et al., 2020; Zhang et al., 2021).
282 Our estimates are on the rise as a whole, but the calculated values are generally lower than those by Zhang
283 et al. (2017) (around 15 Tg N yr⁻¹), but larger than those by EDGAR and Kang et al. (2016).

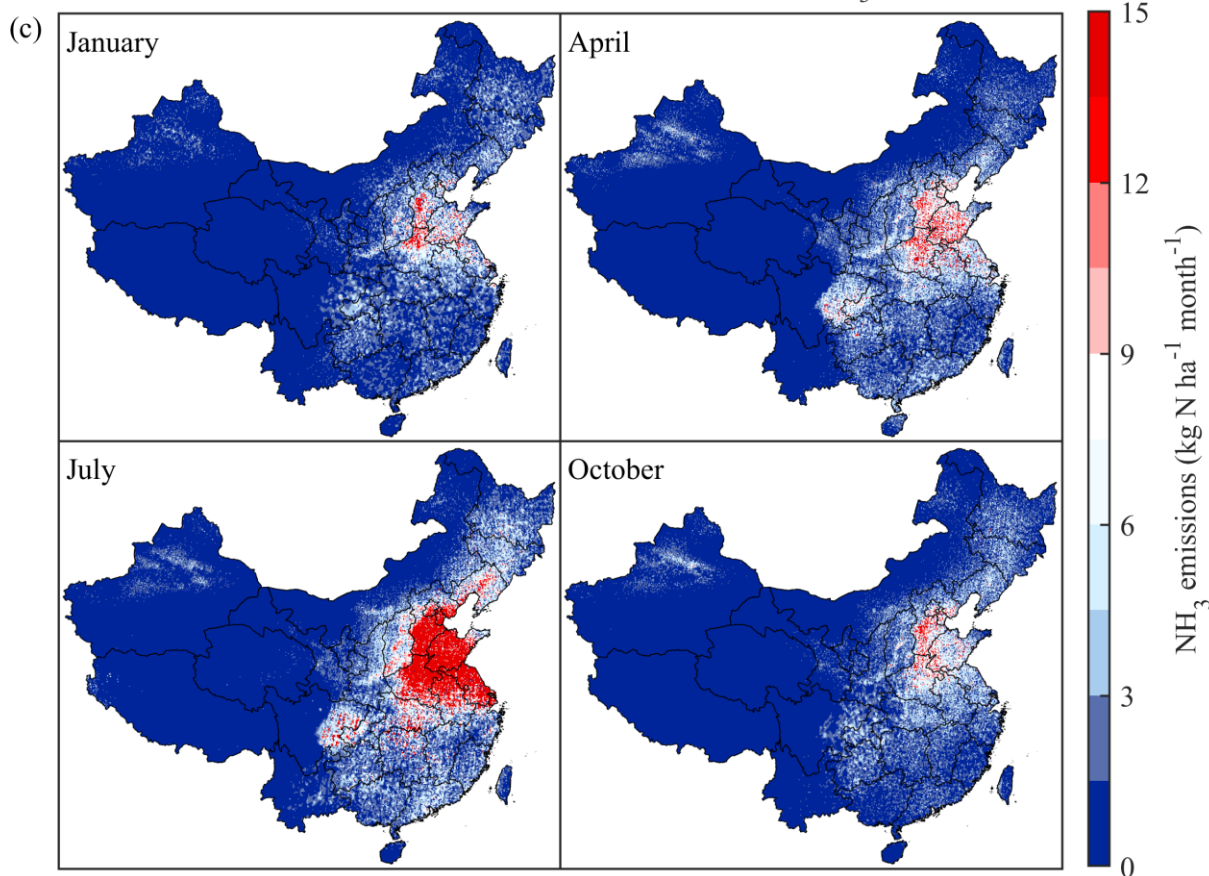
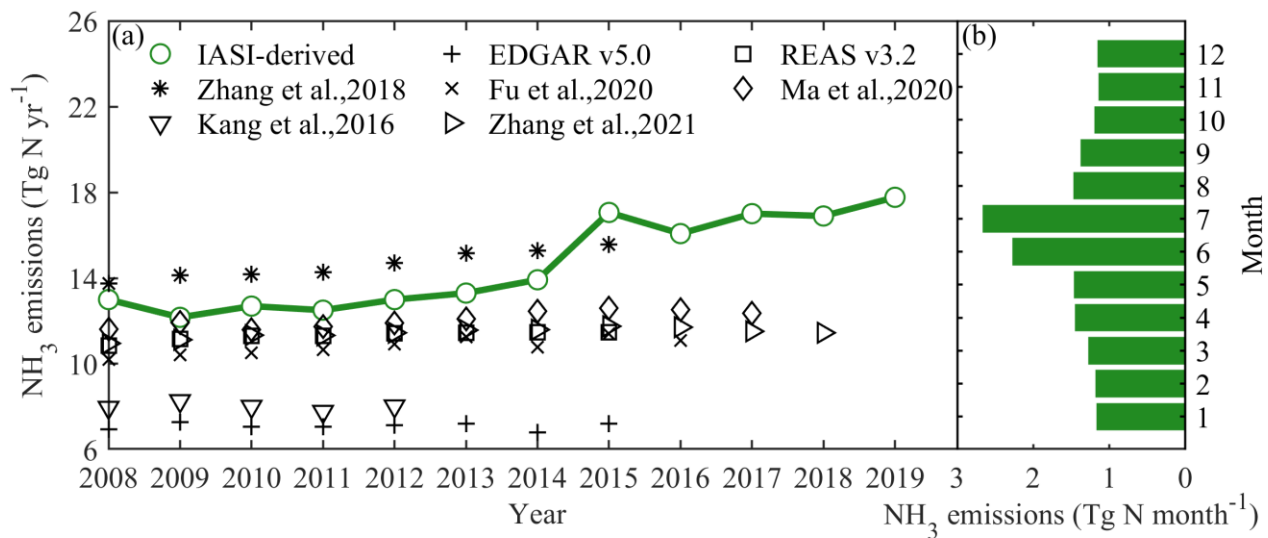
284

285 In terms of spatial distribution, high NH₃ emissions are generally distributed in the North China Plain,
286 Sichuan Basin, Northeast China and Xinjiang, while the low values are mainly distributed in the
287 Southwest China (especially Qinghai-Tibet Plateau). The North China Plain is China's granary, with
288 developed agriculture and animal husbandry, high population densities and strong human activities
289 (including vehicle emissions) (Zhang et al., 2006; Wang et al., 2020). In contrast, South China is rich in
290 rainfall, which promotes the deposition of NH₃ and suppresses its volatilization to a certain extent.

291

292 The spatial distribution of NH₃ emissions in January, April, July and October were selected to characterize
293 the seasonal variations. The average emissions for the four months were 1.15 kg N ha⁻¹, 1.31 kg N ha⁻¹,
294 2.31 kg N ha⁻¹ and 1.16 kg N ha⁻¹ in January, April, July and October, indicating that NH₃ emission is the
295 highest in summer and the lowest in winter. The annual average emission intensity of 2019 is 16.53 kg N
296 ha⁻¹ (0.09-313.47 kg N ha⁻¹). Fig. 8b shows the monthly changes in NH₃ emissions, which basically shows
297 a normal distribution. High values are generally distributed in June and July, and low values are generally
298 distributed in November and December. It reached the maximum monthly emission of 2.6 Tg N m⁻¹ in
299 July 2019 and reached the minimum monthly emission in November and December (1.1 Tg N m⁻¹).

300



301

302 **Figure 8.** Annual changes of NH₃ emissions (a), monthly changes of NH₃ emissions in 2019 (b) and

303 spatial distribution of NH₃ emissions by month in 2019 (c).

304 **4 Limitations and outlook**

305 This study developed satellite-based surface NH_3 concentration and emissions in China based on remote
306 sensing data (IASI and GIIRS). However, several limitations have been identified in this study. First, the
307 Fengyun geostationary satellite used in this study can achieve hourly NH_3 concentrations, but the time
308 series is still very short (2019.11-2020.10), and satellite observations are affected by clouds and
309 meteorological conditions, resulting in missing values in parts of the Yangtze River Basin.

310

311 Second, we used a relatively fixed average conversion ratio (Fig. S2) to estimate surface NH_3
312 concentrations and NH_3 emissions in China, ignoring the time-series variation of the ratio, due to the
313 temporal constraint of emission inventory. In this case, non-emission factors led to higher satellite
314 observed NH_3 column, for example, emission reductions of SO_2 and NO_2 led to increased NH_3 column
315 (Lachatre et al., 2019; Fu et al., 2020), which can introduce uncertainty into NH_3 emission calculations
316 using concentration as the main parameter.

317

318 Third, the spatial resolution of the NH_3 vertical profile simulated by the atmospheric model is relatively
319 coarse (0.5 degrees). In order to make it consistent with the spatial resolution of the remote sensing data,
320 the outputs of GEOS-Chem (vertical profiles and feedback ratio between emissions and surface NH_3
321 concentrations) were interpolated through resampling methods. Owing to the resolution limit, the ratio-
322 based mass balance approach to estimate NH_3 emissions neglected the effects of internal transport of NH_3
323 and displacement of emission sources within the fine grid.

324

325 Finally, there are some uncertainties and biases in the observed NH₃ column by satellite. Earlier versions
326 of the IASI NH₃ column product were 25-50% lower than ground-based measurements (Whitburn et al.,
327 2016; Dammers et al., 2017). However, the new version of IASI v3 lacks a comprehensive ground-based
328 measurement assessment, which has only been compared with limited aircraft observations (Guo et al.,
329 2021). Comparing IASI-derived surface NH₃ concentrations with measurements of ground sites
330 (NNDMN) generally shows consistency in this study. The further work is needed for the complete
331 assessment and error analysis.

332

333 At present, there are more and more satellite sensors (GOSAT, CrIS, AIRS, etc.) that can monitor NH₃
334 concentrations. This study only used IASI and GIIRS, and in the future, data from different satellites can
335 be merged to analyze NH₃ changes on multiple temporal and spatial scales.

336 **5 Conclusion**

337 We use GIIRS to study the NH₃ diel cycle, and estimate surface NH₃ concentrations and emissions based
338 on IASI in China. There are obvious hourly changes in NH₃ concentration in China using GIIRS. Overall,
339 NH₃ concentrations are larger in the daytime than at nighttime in China. Hourly NH₃ concentrations at
340 different land use show different patterns, but high values generally appear in 10:00-16:00. Comparing
341 IASI-derived and observed NH₃ surface concentrations by NNDMN from 2010 to 2015, the coefficient
342 of the fitted line is $1.03 \approx 1$, and the low bias is 2.59%, indicating satellite estimates have good consistency
343 with the measurements. IASI-derived China's NH₃ emissions range from 12.17-17.77 Tg N yr⁻¹ during
344 2008-2019, among which NH₃ emissions increase from 2008 to 2015. The emission intensity of NH₃ in

345 China presents a strong spatial heterogeneity, showing high in the eastern and low in the western. The
346 high values are mainly distributed in the North China Plain and Sichuan Basin. High values are generally
347 distributed in summer, and low values generally occur in winter. This study provides an important
348 reference basis for the formulation of NH₃ pollution prevention and control policy in China.

349 **Data availability**

350 IASI data were obtained from the <https://iasi.aeris-data.fr/nh3/>. The GIRS data were obtained from
351 <https://zenodo.org/record/4540024>.

352 **Author contributions**

353 The study was conceived by LL, and data analysis were performed by JD. The paper was written by PL,
354 with editing from WX and XL. LL was involved in obtaining the project grant and supervised the study.

355 **Competing interests**

356 The contact author has declared that neither they nor their co-authors have any competing interests.

357 **Acknowledgements**

358 This study is supported by the National Natural Science Foundation of China (42001347, 41705130, and
359 41922037) and the Chinese State Key Research & Development Programme (2017YFC0210100,
360 2017YFD0200101). The analysis in this study is supported by the Supercomputing Center of Lanzhou
361 University.

- 363 Cai, X., Bao, Y., Petropoulos, G. P., Lu, F., Lu, Q., Zhu, L., and Wu, Y.: Temperature and humidity profile retrieval from
364 FY4-GIIRS hyperspectral data using artificial neural networks, *Remote Sens.*, 12, 1872, <https://doi.org/10.3390/rs12111872>,
365 2020.
- 366 Clarisse, L., Van Damme, M., Hurtmans, D., Franco, B., Clerbaux, C., and Coheur, P. F.: The diel cycle of NH₃ observed from
367 the FY-4A Geostationary Interferometric Infrared Sounder (GIIRS), *Geophys. Res. Lett.*, 48, e2021GL093010,
368 <https://doi.org/10.1029/2021GL093010>, 2021.
- 369 Cooper, M., Martin, R. V., Padmanabhan, A., and Henze, D. K.: Comparing mass balance and adjoint methods for inverse
370 modeling of nitrogen dioxide columns for global nitrogen oxide emissions, *J. Geophys. Res.: Atmos.*, 122, 4718-4734,
371 <https://doi.org/10.1002/2016JD025985>, 2017.
- 372 Dammers, E., McLinden, C. A., Griffin, D., Shephard, M. W., Graaf, S. V. D., Lutsch, E., Schaap, M., Gainairu-Matz, Y.,
373 Fioletov, V., and Damme, M. V.: NH₃ emissions from large point sources derived from CrIS and IASI satellite observations,
374 *Atmos. Chem. Phys.*, 19, 12261-12293, <https://doi.org/10.5194/acp-19-12261-2019>, 2019.
- 375 Dammers, E., Shephard, M. W., Palm, M., Cady-Pereira, K., Capps, S., Lutsch, E., Strong, K., Hannigan, J. W., Ortega, I.,
376 Toon, G. C., Stremme, W., Grutter, M., Jones, N., Smale, D., Siemons, J., Hrpcek, K., Tremblay, D., Schaap, M., Notholt, J.,
377 and Erisman, J. W.: Validation of the CrIS fast physical NH₃ retrieval with ground-based FTIR, *Atmos. Meas. Tech.*, 10, 2645-
378 2667, <https://doi.org/10.5194/amt-10-2645-2017>, 2017.
- 379 Ding, Y. H., Ren, G. Y., Zhao, Z. C., Xu, Y., Luo, Y., Li, Q. P., and Zhang, J.: Detection, causes and projection of climate
380 change over China: An overview of recent progress, *Adv. Atmos. Sci.*, 24, 954-971, [https://doi.org/10.1007/s00376-007-0954-](https://doi.org/10.1007/s00376-007-0954-4)
381 4, 2007.
- 382 Dong, W., Xing, J., and Wang, S.: Temporal and spatial distribution of anthropogenic ammonia emissions in China: 1994-
383 2006, *Huanjing Kexue*, 31, 1457-1463, 2010.
- 384 Eastham, S. D., Weisenstein, D. K., and Barrett, S. R.: Development and evaluation of the unified tropospheric-stratospheric
385 chemistry extension (UCX) for the global chemistry-transport model GEOS-Chem, *Atmos. Environ.*, 89, 52-63,
386 <https://doi.org/10.1016/j.atmosenv.2014.02.001>, 2014.
- 387 Flechard, C. R., Nemitz, E., Smith, R. I., Fowler, D., Vermeulen, A. T., Bleeker, A., Erisman, J. W., Simpson, D., Zhang, L.,
388 Tang, Y. S., and Sutton, M. A.: Dry deposition of reactive nitrogen to European ecosystems: a comparison of inferential models
389 across the NitroEurope network, *Atmos. Chem. Phys.*, 11, 2703-2728, <https://doi.org/10.5194/acp-11-2703-2011>, 2011.
- 390 Fowler, D., Coyle, M., Skiba, U., Sutton, M. A., Cape, J. N., Reis, S., Sheppard, L. J., Jenkins, A., Grizzetti, B., Galloway, J.
391 N., Vitousek, P., Leach, A., Bouwman, A. F., Butterbach-Bahl, K., Dentener, F., Stevenson, D., Amann, M., and Voss, M.:
392 The global nitrogen cycle in the twenty-first century, *Philos. Trans. R. Soc. B-Biol. Sci.*, 368, 13,
393 <https://doi.org/10.1098/rstb.2013.0164>, 2013.
- 394 Fu, H., Luo, Z., and Hu, S.: A temporal-spatial analysis and future trends of ammonia emissions in China, *Sci. Total Environ.*,
395 731, 138897, <https://doi.org/10.1016/j.scitotenv.2020.138897>, 2020.
- 396 Geddes, J. A. and Martin, R. V.: Global deposition of total reactive nitrogen oxides from 1996 to 2014 constrained with satellite
397 observations of NO₂ columns, *Atmos. Chem. Phys.*, 17, 10071-10091, <https://doi.org/10.5194/acp-17-10071-2017>, 2017.
- 398 Gilliland, A. B., Dennis, R. L., Roselle, S. J., and Pierce, T. E.: Seasonal NH₃ emission estimates for the eastern United States
399 based on ammonium wet concentrations and an inverse modeling method, *J. Geophys. Res.-Atmos.*, 108,
400 <https://doi.org/10.1029/2002jd003063>, 2003.
- 401 Guo, X., Wang, R., Pan, D., Zondlo, M. A., Clarisse, L., Van Damme, M., Whitburn, S., Coheur, P. F., Clerbaux, C., Franco,
402 B., Golston, L. M., Wendt, L., Sun, K., Tao, L., Miller, D., Mikoviny, T., Müller, M., Wisthaler, A., Tevlin, A. G., Murphy, J.
403 G., Nowak, J. B., Roscioli, J. R., Volkamer, R., Kille, N., Neuman, J. A., Eilerman, S. J., Crawford, J. H., Yacovitch, T. I.,
404 Barrick, J. D., and Scarino, A. J.: Validation of IASI satellite ammonia observations at the pixel scale using in situ vertical
405 profiles, *J. Geophys. Res.-Atmos.*, 126, e2020JD033475, <https://doi.org/10.1029/2020jd033475>, 2021.
- 406 He, Y., Pan, Y., Zhang, G., Ji, D., Tian, S., Xu, X., Zhang, R., and Wang, Y.: Tracking ammonia morning peak, sources and
407 transport with 1 Hz measurements at a rural site in North China Plain, *Atmos. Environ.*, 235, 117630,
408 <https://doi.org/10.1016/j.atmosenv.2020.117630>, 2020.
- 409 Huang, X., Song, Y., Li, M., Li, J., Huo, Q., Cai, X., Zhu, T., Hu, M., and Zhang, H.: A high-resolution ammonia emission
410 inventory in China, *Glob. Biogeochem. Cycle*, 26, <https://doi.org/10.1029/2011gb004161>, 2012.

411 Jacob, D. J.: Introduction to atmospheric chemistry, Princeton University Press 1999.

412 Kang, Y., Liu, M., Song, Y., Huang, X., Yao, H., Cai, X., Zhang, H., Kang, L., Liu, X., Yan, X., He, H., Zhang, Q., Shao, M.,
413 and Zhu, T.: High-resolution ammonia emissions inventories in China from 1980 to 2012, *Atmos. Chem. Phys.*, 16, 2043-
414 2058, <https://doi.org/10.5194/acp-16-2043-2016>, 2016.

415 Kong, L., Tang, X., Zhu, J., Wang, Z., Pan, Y., Wu, H., Wu, L., Wu, Q., He, Y., Tian, S., Xie, Y., Liu, Z., Sui, W., Han, L.,
416 and Carmichael, G.: Improved inversion of monthly ammonia emissions in China based on the Chinese ammonia monitoring
417 network and ensemble Kalman filter, *Environ. Sci. Technol.*, 53, 12529-12538, <https://doi.org/10.1021/acs.est.9b02701>, 2019.

418 Kuang, Y., Xu, W., Lin, W., Meng, Z., Zhao, H., Ren, S., Zhang, G., Liang, L., and Xu, X.: Explosive morning growth
419 phenomena of NH₃ on the North China Plain: Causes and potential impacts on aerosol formation, *Environ. Pollut.*, 257, 113621,
420 <https://doi.org/10.1016/j.envpol.2019.113621>, 2020.

421 Kutzner, R. D., Cuesta, J., Chelin, P., Petit, J.-E., Ray, M., Landsheere, X., Tournadre, B., Dupont, J.-C., Rosso, A., Hase, F.,
422 Orphal, J., and Beekmann, M.: Diurnal evolution of total column and surface atmospheric ammonia in the megacity of Paris,
423 France, during an intense springtime pollution episode, *Atmos. Chem. Phys.*, 21, 12091-12111, <https://doi.org/10.5194/acp-21-12091-2021>, 2021.

425 Lachatre, M., Fortems-Cheiney, A., Foret, G., Siour, G., Dufour, G., Clarisse, L., Clerbaux, C., Coheur, P.-F., Van Damme,
426 M., and Beekmann, M.: The unintended consequence of SO₂ and NO₂ regulations over China: increase of ammonia levels and
427 impact on PM 2.5 concentrations, *Atmos. Chem. Phys.*, 19, 6701-6716, <https://doi.org/10.5194/acp-19-6701-2019>, 2019.

428 Lamsal, L., Martin, R., Padmanabhan, A., Van Donkelaar, A., Zhang, Q., Sioris, C., Chance, K., Kurosu, T., and Newchurch,
429 M.: Application of satellite observations for timely updates to global anthropogenic NO_x emission inventories, *Geophys. Res.*
430 *Let.*, 38, <https://doi.org/10.1029/2010GL046476>, 2011.

431 Liu, L., Xu, W., Lu, X., Zhong, B., Guo, Y., Lu, X., Zhao, Y., He, W., Wang, S., Zhang, X., Liu, X., and Vitousek, P.:
432 Exploring global changes in agricultural ammonia emissions and their contribution to nitrogen deposition since 1980, *P. Natl.*
433 *Acad. Sci. USA*, 119, e2121998119, <https://doi.org/10.1073/pnas.2121998119>, 2022.

434 Liu, L., Zhang, X., Wong, A. Y., Xu, W., Liu, X., Li, Y., Mi, H., Lu, X., Zhao, L., Wang, Z., Wu, X., and Wei, J.: Estimating
435 global surface ammonia concentrations inferred from satellite retrievals, *Atmos. Chem. Phys.*, 19, 12051-12066,
436 <https://doi.org/10.5194/acp-19-12051-2019>, 2019.

437 Ma, S.: High-resolution assessment of ammonia emissions in China: Inventories, driving forces and mitigation, *Atmos.*
438 *Environ.*, 229, 117458, <https://doi.org/10.1016/j.atmosenv.2020.117458>, 2020.

439 Marais, E. A., Pandey, A. K., Van Damme, M., Clarisse, L., Coheur, P. F., Shephard, M. W., Cady-Pereira, K. E., Misselbrook,
440 T., Zhu, L., Luo, G., and Yu, F.: UK Ammonia Emissions Estimated With Satellite Observations and GEOS-Chem, *J. Geophys.*
441 *Res.-Atmos.*, 126, e2021JD035237, <https://doi.org/10.1029/2021JD035237>, 2021.

442 Paerl, H. W., Gardner, W. S., McCarthy, M. J., Peierls, B. L., and Wilhelm, S. W.: Algal blooms: noteworthy nitrogen, *Science*,
443 346, 175-175, <https://doi.org/10.1126/science.346.6206.175-a>, 2014.

444 Pan, Y., Tian, S., Zhao, Y., Zhang, L., Zhu, X., Gao, J., Huang, W., Zhou, Y., Song, Y., and Zhang, Q.: Identifying ammonia
445 hotspots in China using a national observation network, *Environ. Sci. Technol.*, 52, 3926-3934,
446 <https://doi.org/10.1021/acs.est.7b05235>, 2018.

447 Pandolfi, M., Amato, F., Reche, C., Alastuey, A., Otjes, R. P., Blom, M. J., and Querol, X.: Summer ammonia measurements
448 in a densely populated Mediterranean city, *Atmos. Chem. Phys.*, 12, 7557-7575, <https://doi.org/10.5194/acp-12-7557-2012>,
449 2012.

450 Paulot, F., Jacob, D. J., Pinder, R. W., Bash, J. O., Travis, K., and Henze, D. K.: Ammonia emissions in the United States,
451 European Union, and China derived by high-resolution inversion of ammonium wet deposition data: Interpretation with a new
452 agricultural emissions inventory (MASAGE_NH3), *J. Geophys. Res.-Atmos.*, 119, 4343-4364,
453 <https://doi.org/10.1002/2013jd021130>, 2014.

454 Peng, S., Huang, J., Zhong, X., Yang, J., Wang, G., Zou, Y., Zhang, F., Zhu, Q., Buresh, R., and Witt, C.: Challenge and
455 opportunity in improving fertilizer-nitrogen use efficiency of irrigated rice in China, *Agric. Sci. China*, 1, 776-785, 2002.

456 Pinder, R. W., Walker, J. T., Bash, J. O., Cady-Pereira, K. E., Henze, D. K., Luo, M. Z., Osterman, G. B., and Shephard, M.
457 W.: Quantifying spatial and seasonal variability in atmospheric ammonia with in situ and space-based observations, *Geophys.*
458 *Res. Lett.*, 38, 5, <https://doi.org/10.1029/2010gl046146>, 2011.

459 Shephard, M. W. and Cady-Pereira, K. E.: Cross-track Infrared Sounder (CrIS) satellite observations of tropospheric ammonia,
460 *Atmos. Meas. Tech.*, 8, 1323-1336, <https://doi.org/10.5194/amt-8-1323-2015>, 2015.

461 Someya, Y., Imasu, R., Shiomi, K., and Saitoh, N.: Atmospheric ammonia retrieval from the TANSO-FTS/GOSAT thermal
462 infrared sounder, *Atmos. Meas. Tech.*, 13, 309-321, <https://doi.org/10.5194/amt-13-309-2020>, 2020.

463 Van Damme, M., Whitburn, S., Clarisse, L., Clerbaux, C., Hurtmans, D., and Coheur, P.-F.: Version 2 of the IASI NH₃ neural
464 network retrieval algorithm: near-real-time and reanalysed datasets, *Atmos. Meas. Tech.*, 10, 4905-4914,
465 <https://doi.org/10.5194/amt-10-4905-2017>, 2017.

466 Van Damme, M., Clarisse, L., Whitburn, S., Hadji-Lazaro, J., Hurtmans, D., Clerbaux, C., and Coheur, P. F.: Industrial and
467 agricultural ammonia point sources exposed, *Nature*, 564, 99-103, <https://doi.org/10.1038/s41586-018-0747-1>, 2018.

468 Van Damme, M., Clarisse, L., Heald, C. L., Hurtmans, D., Ngadi, Y., Clerbaux, C., Dolman, A., Erisman, J. W., and Coheur,
469 P.-F.: Global distributions, time series and error characterization of atmospheric ammonia (NH₃) from IASI satellite
470 observations, *Atmos. Chem. Phys.*, 14, 2905-2922, <https://doi.org/10.5194/acp-14-2905-2014>, 2014.

471 Wang, S., Nan, J., Shi, C., Fu, Q., Gao, S., Wang, D., Cui, H., Saiz-Lopez, A., and Zhou, B.: Atmospheric ammonia and its
472 impacts on regional air quality over the megacity of Shanghai, China, *Sci. Rep.-UK*, 5, 1-13, <https://doi.org/10.1038/srep15842>,
473 2015.

474 Wang, Z., Zhang, X., Liu, L., Cheng, M., and Xu, J.: Spatial and seasonal patterns of atmospheric nitrogen deposition in North
475 China, *Atmospheric and Oceanic Science Letters*, 13, 188-194, <https://doi.org/10.1080/16742834.2019.1701385>, 2020.

476 Warner, J. X., Wei, Z. G., Strow, L. L., Dickerson, R. R., and Nowak, J. B.: The global tropospheric ammonia distribution as
477 seen in the 13-year AIRS measurement record, *Atmos. Chem. Phys.*, 16, 5467-5479, [https://doi.org/10.5194/acp-16-5467-](https://doi.org/10.5194/acp-16-5467-2016)
478 2016, 2016.

479 Werner, M., Kryza, M., Geels, C., Ellermann, T., and Skjøth, C. A.: Ammonia concentrations over Europe—application of the
480 WRF-Chem model supported with dynamic emission, *Pol. J. Environ. Stud.*, 26, 1323-1341,
481 <https://doi.org/10.15244/pjoes/67340>, 2017.

482 Wesely, M.: Parameterization of surface resistances to gaseous dry deposition in regional-scale numerical models, *Atmos.*
483 *Environ.*, 41, 52-63, <https://doi.org/10.1016/j.atmosenv.2007.10.058>, 2007.

484 Whitburn, S., Van Damme, M., Clarisse, L., Bauduin, S., Heald, C., Hadji-Lazaro, J., Hurtmans, D., Zondlo, M. A., Clerbaux,
485 C., and Coheur, P. F.: A flexible and robust neural network IASI-NH₃ retrieval algorithm, *J. Geophys. Res.-Atmos.*, 121,
486 6581-6599, <https://doi.org/10.1002/2016JD024828>, 2016.

487 Xu, W., Luo, X. S., Pan, Y. P., Zhang, L., Tang, A. H., Shen, J. L., Zhang, Y., Li, K. H., Wu, Q. H., Yang, D. W., Zhang, Y.
488 Y., Xue, J., Li, W. Q., Li, Q. Q., Tang, L., Lu, S. H., Liang, T., Tong, Y. A., Liu, P., Zhang, Q., Xiong, Z. Q., Shi, X. J., Wu,
489 L. H., Shi, W. Q., Tian, K., Zhong, X. H., Shi, K., Tang, Q. Y., Zhang, L. J., Huang, J. L., He, C. E., Kuang, F. H., Zhu, B.,
490 Liu, H., Jin, X., Xin, Y. J., Shi, X. K., Du, E. Z., Dore, A. J., Tang, S., Collett, J. L., Goulding, K., Sun, Y. X., Ren, J., Zhang,
491 F. S., and Liu, X. J.: Quantifying atmospheric nitrogen deposition through a nationwide monitoring network across China,
492 *Atmos. Chem. Phys.*, 15, 12345-12360, <https://doi.org/10.5194/acp-15-12345-2015>, 2015.

493 Zhang, L., Chen, Y. F., Zhao, Y. H., Henze, D. K., Zhu, L. Y., Song, Y., Paulot, F., Liu, X. J., Pan, Y. P., Lin, Y., and Huang,
494 B. X.: Agricultural ammonia emissions in China: reconciling bottom-up and top-down estimates, *Atmos. Chem. Phys.*, 18,
495 339-355, <https://doi.org/10.5194/acp-18-339-2018>, 2018.

496 Zhang, Q., Yu, Y., Zhang, W., Luo, T., and Wang, X.: Cloud detection from FY-4A's geostationary interferometric infrared
497 sounder using machine learning approaches, *Remote Sens.*, 11, 3035, <https://doi.org/10.3390/rs11243035>, 2019.

498 Zhang, X., Wu, Y., Liu, X., Reis, S., Jin, J., Dragosits, U., Van Damme, M., Clarisse, L., Whitburn, S., Coheur, P.-F. o., and
499 Gu, B.: Ammonia emissions may be substantially underestimated in China, *Environ. Sci. Technol.*, 51, 12089-12096,
500 <https://doi.org/10.1021/acs.est.7b02171>, 2017.

501 Zhang, X. M., Ren, C. C., Gu, B. J., and Chen, D. L.: Uncertainty of nitrogen budget in China, *Environ. Pollut.*, 286, 9,
502 <https://doi.org/10.1016/j.envpol.2021.117216>, 2021.

503 Zhang, Y., Liu, X., Zhang, F., Ju, X., Zou, G., and Hu, K.: Spatial and temporal variation of atmospheric nitrogen deposition
504 in the North China Plain, *Acta Ecologica Sinica*, 26, 1633-1638, [https://doi.org/10.1016/S1872-2032\(06\)60026-7](https://doi.org/10.1016/S1872-2032(06)60026-7), 2006.

505 Zhou, F., Ciais, P., Hayashi, K., Galloway, J., Kim, D.-G., Yang, C., Li, S., Liu, B., Shang, Z., and Gao, S.: Re-estimating
506 NH₃ emissions from Chinese cropland by a new nonlinear model, *Environ. Sci. Technol.*, 50, 564-572,
507 <https://doi.org/10.1021/acs.est.5b03156>, 2016.